

Quantum transport at the Dirac point: Mapping out the minimum conductivity from pristine to disordered graphene

Redwan N. Sajjad

*Department of Electrical Engineering and Computer Science,
Massachusetts Institute of Technology, Cambridge, MA-02139, USA.*

Frank Tseng

Naval Research Laboratory, Washington D.C. 20375, USA.

K. M. Masum Habib and Avik W. Ghosh

Department of Electrical and Computer Engineering, University of Virginia, VA 22904, USA.

(Dated: July 31, 2018)

The phase space for graphene's minimum conductivity σ_{\min} is mapped out using Landauer theory modified for scattering using Fermi's Golden Rule, as well as the Non-Equilibrium Green's Function (NEGF) simulation with a Monte Carlo sampling over impurity distributions. The resulting 'fan diagram' spans the range from ballistic to diffusive over varying aspect ratios (W/L), and bears several surprises. The device aspect ratio determines how much tunneling (between contacts) is allowed and becomes the dominant factor for the evolution of σ_{\min} from ballistic to diffusive regime. We find an increasing (for $W/L > 1$) or decreasing ($W/L < 1$) trend in σ_{\min} vs. impurity density, all converging around $128q^2/\pi^3h \sim 4q^2/h$ at the dirty limit. In the diffusive limit, the conductivity quasi-saturates due to the precise cancellation between the increase in conducting modes from charge puddles vs the reduction in average transmission from scattering at the Dirac Point. In the clean ballistic limit, the calculated conductivity of the lowest mode shows a surprising absence of Fabry-Pérot oscillations, unlike other materials including bilayer graphene. We argue that the lack of oscillations even at low temperature is a signature of Klein tunneling.

Since its discovery in the last decade, single layer graphene has catalyzed widespread research¹ stemming from its extraordinary material properties. Multiple electronic, spintronic and opto-electronic applications are predicted to arise from the entire class of 2D materials emergent in graphene's footsteps². Despite intense scrutiny, there exist many unresolved issues that continue to make the material fascinating. Among them is the physics of the minimum conductivity, σ_{\min} around the Dirac point, where the density of states is expected to vanish. Instead of vanishing accordingly, σ_{\min} for a ballistic sheet with large width to length aspect ratio ($W/L \gg 1$) is shown to be a universal constant $\sigma_Q = 4q^2/\pi h$ ^{3,4}. This arises from the preponderance of tunneling through a continuum of subbands with near zero bandgaps. In these structures ($W \gg L$ samples), a series of exponentially decaying tunnel transmissions adds up to an overall Ohmic term that factors out of the ballistic conductance $G = \sigma W/L$. Measured σ_{\min} s, however, are typically in the range $4 - 12q^2/h$ ^{5,7-9}, except Ref.³, larger than σ_Q . This is surprising given that these experiments are mostly on dirty samples where we expect the conductivity to be not only non-universal, but certainly smaller than the ballistic limit. The increase in σ_{\min} from σ_Q arises from charged impurities on the substrates that create electron and hole puddles and contribute states to the charge neutrality point¹⁰. However an opposite, decreasing trend of σ_{\min} vs. impurity concentration (n_{imp}) was demonstrated theoretically by Adam *et.al.* in Ref.⁶ within Boltzmann transport theory, as well as experimentally in Ref.⁵. Clearly there are sev-

eral disjointed pieces that have yet to come together to provide a complete phase picture of the evolution of σ_{\min} with sample quality.

In this paper, we use quasi-analytical Landauer equation as well as numerical NEGF (within the Fisher-Lee formulation)¹⁴ to map out the entire phase space of σ_{\min} for varying n_{imp} and W/L (Fig. 1). Our results clearly show that the missing link is the total tunneling current (a function of W/L), a piece of physics typically ignored in semi-classical models. The observed quasi-saturation arises due to a trade-off between the number of modes and the scattering time τ from charge puddles, as we move from the ballistic to diffusive regime. The total conductivity can be written as

$$\sigma = G_0 [M_p T_p + M_e T_e] \times L/W \quad (1)$$

where $G_0 = 4q^2/h$ is conductance quantum including spin and valley degeneracy, M_p and M_e are the number of propagating and evanescent modes and T is the corresponding mode averaged transmission probability. While this equation defines an absolute lower bound on conductivity at $\sigma_Q = 4q^2/\pi h$ (dashed line in Fig. 1 top), we will shortly show that for dirty samples with impurity density $\sim 3 - 5 \times 10^{12}/\text{cm}^2$, it predicts a quasi-saturating $\sigma_{\min} \approx 4q^2/h$, consistent with experiments (Fig. 1). Part of the fan diagram for $W \ll L$, the decreasing trend in σ_{\min} in Fig. 1 obtained earlier using Boltzmann transport equation, arises naturally in our model from scattering of the propagating modes $\sigma \propto \mathcal{G}_0 [M_p T_p]$, where $M_p T_p \propto \sqrt{n_0^2 + n_{\text{imp}}^2}/n_{\text{imp}} = \sqrt{1 + n_0^2/n_{\text{imp}}^2}$ (n_0

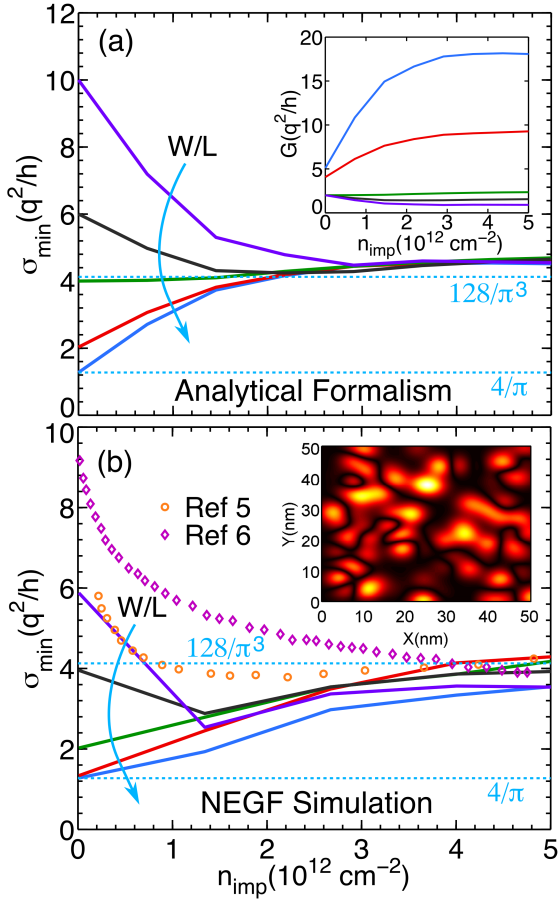


FIG. 1. (Color online) (a) Fan diagram of quasi-analytical σ_{\min} for $W = 500$ nm with varying W/L (inset shows conductance G). The ballistic σ_{\min} is exactly at $\sigma_Q = 4q^2/\pi h$. The two new features are (1) quasi-saturation at high impurity density to $\sim 128q^2/\pi^3 h$ and (2) a flip in curvature between aspect ratios. (b) NEGF calculated σ_{\min} averaged over puddle geometries (inset). The data saturate at $\sim 4q^2/h$ in dirty graphene. Dotted green curve is experimental data from Ref.⁵ and open circles are theoretical predictions from Ref.⁶

is the background doping). For the opposite ballistic limit, wide samples have a conductivity that dips down to the quantized value σ_Q to generate the rest of the fan diagram. At the same time, narrow ballistic samples with limited tunneling show a *conductance* quantization \mathcal{G}_0 that bears a spectacular robustness with temperature and a remarkable absence of Fabry Péro (FP) resonance even at low temperature. We interpret the absence of FP (Fig. 3) as a clear signature of Klein tunneling, where the linear relativistic electron transmits perfectly at normal incidence due to pseudospin conservation, contrary to the prediction of nonrelativistic Schrödinger equation (which applies to Bilayer graphene as we show). Our results are supported by numerical NEGF sampled over a Monte Carlo distribution of charged impurities.

Modeling charged impurities: The lack of dangling bonds makes direct chemisorption of charged impuri-

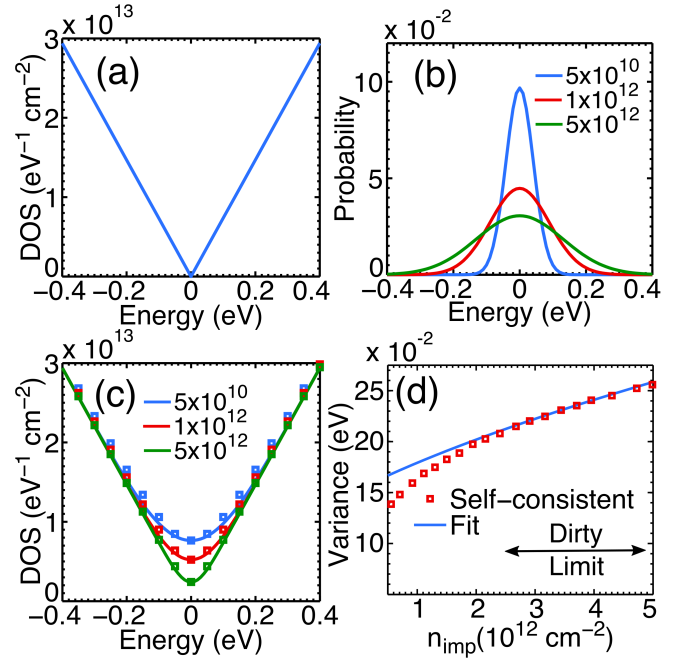


FIG. 2. Averaging (a) the pristine graphene density of states with (b) a normal distribution of random potentials (c) erases the Dirac point. (d) The variance of the Gaussian is calculated self-consistently and refitted with a simplified expression, closely matching with the self-consistent calculation in the dirty limit.

ties difficult on graphene. However, dielectric substrates can have charged impurities that play a significant role on transport around graphene's Dirac point. The physisorption of charged impurities randomly dopes the graphene, creating a Gaussian distribution in energy of Dirac points around neutrality. The resulting erasure of the Dirac point is already seen in quantum capacitance measurements¹¹. We can average the linear density of states of graphene (Fig. 2a) over a Gaussian distribution of potentials (Fig. 2b), with average potential zero, variance σ_E , and potential U_i at the i th location. The exact expression involving error functions was worked out by Li *et al.*¹², but we can express it in a simpler form that interpolates between the low-energy parabolic and high energy linear behavior (Fig. 2c).

$$D_{\text{puddle}}(E) = \frac{2\sqrt{\frac{2}{\pi}}\sigma_E e^{-E^2/2\sigma_E^2} + 2|E|\text{erf}\left(\frac{|E|}{\sigma_E\sqrt{2}}\right)}{\pi\hbar^2 v_F^2}$$

$$D_{\text{puddle}} \approx \frac{2\sqrt{E^2 + 2\sigma_E^2}/\pi}{\pi\hbar^2 v_F^2} \quad (2)$$

Eq. 2 shows that the variance σ_E has a direct impact on the minimum density of states. Fig. 2d shows that σ_E increases with charged impurity concentration, so that *the minimum number of modes for conduction is proportional to the statistical variance of charge impurities*. This has also been worked out by solving Poisson's equation in

cylindrical coordinates¹²

$$\sigma_E^2 = 2\pi n_{\text{imp}} q^2 \int [A_k]^2 k dk \quad (3)$$

$$A_k = \frac{2e^{-\kappa z_0} Z q \sinh(kd)}{k\kappa_{\text{ins}} \cosh(kd) + (k\kappa_v + 2q_{TF}\kappa) \sinh(kd)} \quad (4)$$

κ_v and κ_{ins} are the respective vacuum and insulator dielectric constants, while κ is their average. And $q_{TF} = 2\pi q^2/\kappa D_{\text{puddle}}(E)$ is the Thomas-Fermi screening wavevector which depends on the average density of states (Eq. 2). A_k is the potential solved from Poisson's equation which accounts for the distance of the impurities (z_0) inside the oxide, thickness of the oxide (d) and the screening length ($1/q_{TF}$). Solved self-consistently (between σ_E and D_{puddle}) we determine the variance of the normal distribution of potentials (Fig. 2d). Over the dirty range, we can simplify it with a fitted equation

$$\sigma_E^2 \approx 2\hbar^2 v_F^2 n_{\text{imp}} + C \quad (5)$$

where $C = 0.027eV^2$. This equation closely approximates the self-consistent calculation at the dirty limit. The variation of σ_{min} in presence of charged impurities allows us to quantify the competition between increasing modes and increased scattering.

Analytical Model for σ_{min} . The Landauer conductivity intuitively frames conduction as proportional to the transmission probability of electrons, T_n , summed over all propagating and evanescent modes, where n is the mode index. $\sigma_{\text{min}} = GL/W = 4q^2/h \sum_{n=0}^{\infty} T_n L/W$. The general form for T_n , derivable by matching the pseudospin wavefunctions across an n - p - n or p - n - p junction with barrier height U_0 gives¹³ $T_n = \left| \frac{k_n}{k_n \cos k_n L + i(U_0/\hbar v_F) \sin k_n L} \right|^2$ where $k_n = \sqrt{(U_0/\hbar v_F)^2 - q_n^2}$ and $q_n = n\pi/W$ is the transverse wave-vector in the channel that we sum over to get the total transmission. When k_n is real then the transverse modes are propagating, while when k_n is imaginary they become evanescent. Imaginary k_n changes all the trigonometric functions to hyperbolic functions giving us an evanescent transmission $T_e = 1/\cosh^2 q_n L$ when U_0 is zero. An integral over a continuum of such cosh contributions gives an overall factor of $W/\pi L$ which leads to the ballistic conductivity quantization (σ_Q). For propagating modes, the transmission probability T_p picks up an additional scattering coefficient term from a series sum over the multiple scattering history, $\lambda/(\lambda+L)$, where λ is the electron mean free path in the presence of embedded impurities. The mean free path is $v_F \tau_{sc}$ where the momentum scattering time τ_{sc} is determined from Fermi's Golden Rule below. Combining all the elements in Eq. 1, we arrive at the fan diagram in Fig. 1.

Impurity scattering occurs through a 2D screened Coulomb energy, given at long wavelength by the Thomas Fermi equation, $V_C(\mathbf{r}) = q^2/(4\pi\epsilon_0 r)e^{-\kappa r}$. Using the pseudospin eigenstates, $\Psi_{i,f}(\mathbf{r}) =$

$1/\sqrt{2S} (1 \ e^{i\theta_{i,f}})^T e^{i\mathbf{k}_i \cdot \mathbf{r}}$ normalized over area S , we calculate the scattering matrix element $V_{i,f} = \int d^2\mathbf{r} \Psi_f^*(\mathbf{r}) V_C(\mathbf{r}) \Psi_i(\mathbf{r})$. In terms of scattering wavevector and angle $\Delta\mathbf{k} = \mathbf{k}_f - \mathbf{k}_i$, $\Delta\theta = \theta_f - \theta_i$,

$$V_{i,f} = \frac{q^2}{4\epsilon_0 S \sqrt{\Delta k^2 + \kappa^2}} \left[1 + e^{i\Delta\theta} \right] \quad (6)$$

We can change to energy variables for elastic scattering using $|\mathbf{k}_f| = |\mathbf{k}_i| = E/(\hbar v_F)$, $(\Delta k)^2 = |\mathbf{k}_f - \mathbf{k}_i|^2 = k_f^2 + k_i^2 - 2k_f k_i \cos \Delta\theta = 2E^2(1 - \cos \Delta\theta)/(\hbar^2 v_F^2)$. For an impurity density n_{imp} and cross sectional area S (i.e., number of impurities $n_{\text{imp}} S$), Fermi's Golden rule now gives us, $\hbar/\tau_{sc} = \sum_{\mathbf{f}} |V_{i,f}|^2 \delta(E - E_k) (1 - \cos \theta_k) n_{\text{imp}} S$. Converting sum into integral using the density of states (Eq. 2), and using the calculated expression for $|V_{i,f}|^2$ simplified for low energies, we get

$$\frac{\hbar}{\tau_{sc}} = \frac{q^4 \hbar^2 v_F^2 n_{\text{imp}}}{16\epsilon_0^2 \pi} \int D_{\text{puddle}}(E_k) dE_k \delta(E - E_k) \times \int d\Delta\theta \frac{1 - \cos^2 \Delta\theta}{2E_k^2 (1 - \cos \Delta\theta) + \hbar^2 v_F^2 \kappa^2} \quad (7)$$

The cosine integral followed by the delta function energy integral gives us

$$\frac{\hbar}{\tau_{sc}} = \frac{q^4 \hbar^2 v_F^2 n_{\text{imp}}}{16\epsilon_0^2 \pi} D_{\text{puddle}}(E) \frac{\pi}{2E^4} \times \left[2E^2 + \hbar^2 v_F^2 \kappa^2 - \hbar v_F \kappa \sqrt{4E^2 + \hbar^2 v_F^2 \kappa^2} \right] \quad (8)$$

with D_{puddle} defined in Eq. 2. For $E \ll \hbar v_F \kappa$, the term in square brackets expands to $2E^4/\hbar^2 v_F^2 \kappa^2 + O(E^6/\hbar^4 v_F^4 \kappa^4)$. We then get

$$\frac{\hbar}{\tau_{sc}} \approx \frac{q^4 n_{\text{imp}} D_{\text{puddle}}}{16\epsilon_0^2 \kappa^2} \quad (9)$$

with $\kappa = q^2 D_{\text{puddle}}/\epsilon_0$, giving us $\hbar/\tau_{sc} = (n_{\text{imp}}/16) D_{\text{puddle}}$. Using the Einstein relation (diffusion coefficient $\mathcal{D} = v_F^2 \tau_{sc}/2$), we get

$$\sigma_{\text{min}} = q^2 D_{\text{puddle}} \mathcal{D} = \frac{8q^2 v_F^2 \hbar}{n_{\text{imp}}} D_{\text{puddle}}^2 \quad (10)$$

At high impurity density, $D_{\text{puddle}}^2 \approx 8\sigma_E^2/\pi^3 \hbar^4 v_F^4$ (Eq. 2). Using the approximate relation from Eq. 5 matching the self-consistent calculation fairly well in the dirty limit (Fig. 2), we get

$$\lim_{n_{\text{imp}} \rightarrow \infty} \sigma_{\text{min}} \approx \frac{128q^2}{\pi^3 \hbar} = 4.12 \frac{q^2}{\hbar} \quad (11)$$

Numerical model for σ_{min} : We now show NEGF based numerical simulation results to calculate σ_{min} in presence of charged impurities. We implement a discretized \mathbf{k}, \mathbf{p} Hamiltonian (H) to expedite computation. We use a

sequence of Gaussian potential profiles for the impurity scattering centers,

$$U(r) = \sum_{n=1}^{n_{\text{imp}}} U_n \exp(-|r - r_n|^2/2\zeta^2) \quad (12)$$

specifying the strength of the impurity potential at atomic site r , with r_n being the positions of the impurity atoms and ζ the screening length (~ 3 nm). The amplitudes U_n are random numbers following a Gaussian distribution with a standard deviation of 100meV ⁸. This standard deviation is to be differentiated from the standard deviation in the density of states description (Eq. 2), which is a lumped description for the entire sheet instead of individual impurities. The Gaussian profile (Eq. 12) is used to prevent the potential from going to infinity at the scattering centers (Thomas-Fermi) and such approach is widely employed in the literature^{8,15–18}. With U added to H , we calculate σ_{min} as a function n_{imp} (Fig. 1b) by calculating average conductance over ~ 800 random impurity configurations. In the ballistic limit, σ_{min} varies linearly with L/W , but as the sample gets dirtier, the σ_{min} becomes less dependent on L/W . At high impurity limit, σ_{min} becomes weakly dependent on n_{imp} and saturates around $4q^2/h$. In most experiments, the device length L is larger than width W and therefore see a decreasing trend for σ_{min} vs. n_{imp} such as Ref.⁵. The evolution of σ_{min} from $4q^2/\pi h$ to $\sim 4q^2/h$ and therefore the missing π can only be seen for devices with $W \gg L$. The differences between the numerical and the analytical approaches most likely originate from the lack of adequate samples.

Absence of Fabry-Pérot as a signature of Klein tunneling: Due to non-uniform doping along the metal-graphene-metal captured in our model by the differential dopings, a Fabry-Pérot cavity is formed. Such a cavity leads to quantum interference oscillations and conductance asymmetry (n - n - n vs. n - p - n doping), seen in Fig. 3 in the ballistic limit. Such oscillations have been seen experimentally at low temperature in 2DEGs¹⁹, but are conspicuously missing for the lowest mode in single layer graphene (SLG), as seen in Fig. 3 left column. In contrast, the higher modes in the same column show oscillations, as do all the modes for bilayer graphene (BLG) seen in the right column. The lowest mode in single layer graphene has forward and reverse propagating $E-k$ bands with opposite pseudospin indices (bonding vs antibonding combinations of dimer p_z orbitals) that disallow any reflection at heterojunctions. The resulting Klein tunneling²⁰ makes the heterojunctions completely transparent to the lowest propagating modes and eliminates any Fabry-Pérot oscillations. The parabolic lowest bands of BLG have twice the winding number around the Fermi circle (angle $2\theta_{i,f}$ in the pseudospin eigenstate $\Psi_{i,f}$) and thus a common pseudospin index, leading to finite reflection and Fabry-Pérot oscillations.

We thus expect distinct behaviors of σ_{min} vs. L/W

in single layer and bilayer graphene. For large L/W ,

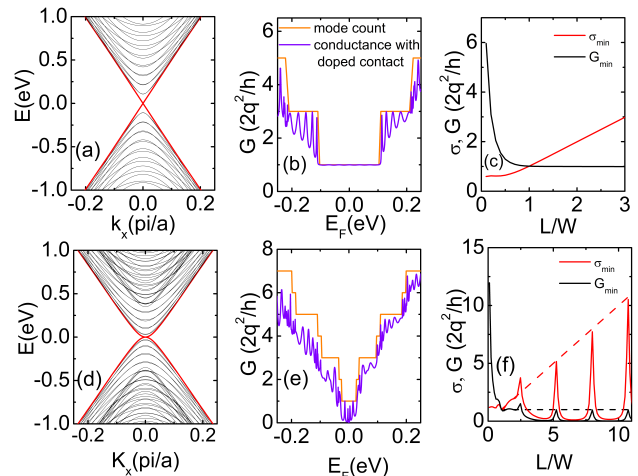


FIG. 3. (Color online) NEGF calculation of total conductance G of single layer graphene and bilayer graphene reveals the nature of Fabry-Pérot oscillation for the lowest mode. a, d shows linear and parabolic $E - K$ in single layer and bilayer graphene. The lowest mode in single layer does not show any oscillation (b) but the bilayer does (e). The variation of minimum conductance and conductivity for single layer shows saturating G_{min} at $2q^2/h$ (c), while for bilayer graphene the minimum conductance never saturates and produces oscillation in both G_{min} and σ_{min} (f).

G_{min} for SLG approaches $2q^2/h$ eliminating all tunneling modes from source to drain and $\sigma_{\text{min}} = GL/W$ increases linearly (Fig. 3(a-c), already demonstrated in experiment³. For BLG (Fig. 3d-f), the conductance oscillation for the lowest mode is manifested in the length dependence as well, leading to an oscillation in both G_{min} and σ_{min} . For small L/W , the σ_{min} saturates to $4q^2/(\pi h)$ and $2q^2/h$ for SLG and BLG respectively^{13,21}. Such non-trivial transport behavior near the Dirac point is a measurable signature of Klein tunnel and reflection.

Conclusion: The composite phase plot of graphene's minimum conductivity is presented within a unified Landauer-Fermi's golden rule and NEGF transport model. We show a general convergence of σ_{min} vs. impurity concentration along with a quasi-saturation at high impurity concentration to $\sim 4q^2/h$ irrespective of device dimensions. For high aspect ratios the increase in density of states due to charged impurities results in a logarithmically increasing σ_{min} from the ballistic limit. On the other hand for low aspect ratios, the scattering due to charged impurities dominates and results in a power law decrease in the σ_{min} . For clean samples with conductance quantization, gating the sample into its lowest mode reveals a striking absence of low-temperature Fabry-Pérot oscillations at low temperatures for SLG but not BLG, providing a signature of Klein tunneling.

Acknowledgement: This work was financially supported by the NRI-INDEX center. The authors thank Eugene Kolomeisky (UVA) for useful discussions.

-
- ¹ A. K. Geim and K. S. Novoselov, *Nature materials* **6**, 183 (2007).
 - ² G. Fiori, F. Bonaccorso, G. Iannaccone, T. Palacios, D. Neumaier, A. Seabaugh, S. K. Banerjee, and L. Colombo, *Nature nanotechnology* **9**, 768 (2014).
 - ³ F. Miao, S. Wijeratne, Y. Zhang, U. C. Coskun, W. Bao, and C. N. Lau, *Science* **317**, 1530 (2007).
 - ⁴ J. Tworzydło, I. Snyman, A. R. Akhmerov, and C. W. J. Beenakker, *Phys. Rev. B* **76**, 035411 (2007).
 - ⁵ J.-H. Chen, C. Jang, S. Adam, M. S. Fuhrer, E. D. Williams, and M. Ishigami, *Nat Phys* **4**, 377 (2008).
 - ⁶ S. Adam, E. Hwang, V. Galitski, and S. Das Sarma, *Proceedings of the National Academy of Sciences* **104**, 18392 (2007).
 - ⁷ Y.-W. Tan, Y. Zhang, K. Bolotin, Y. Zhao, S. Adam, E. H. Hwang, S. Das Sarma, H. L. Stormer, and P. Kim, *Phys. Rev. Lett.* **99**, 246803 (2007).
 - ⁸ Y. Sui, T. Low, M. Lundstrom, and J. Appenzeller, *Nano letters* **11**, 1319 (2011).
 - ⁹ F. Amet, J. Williams, K. Watanabe, T. Taniguchi, and D. Goldhaber-Gordon, *Physical Review Letters* **110**, 216601 (2013).
 - ¹⁰ J. Martin, N. Akerman, G. Ulbricht, T. Lohmann, J. Smet, K. Von Klitzing, and A. Yacoby, *Nature Physics* **4**, 144 (2007).
 - ¹¹ Y. Zhang, V. W. Brar, C. Girit, A. Zettl, and M. F. Crommie, *Nature Physics* **5**, 722 (2009).
 - ¹² Q. Li, E. Hwang, and S. D. Sarma, *Physical Review B* **84**, 115442 (2011).
 - ¹³ J. Tworzydło, B. Trauzettel, M. Titov, A. Rycerz, and C. W. J. Beenakker, *Phys. Rev. Lett.* **96**, 246802 (2006).
 - ¹⁴ S. Datta, *Quantum transport: atom to transistor* (Cambridge University Press, 2005).
 - ¹⁵ J. W. Kłos and I. V. Zozoulenko, *Phys. Rev. B* **82**, 081414 (2010).
 - ¹⁶ C. H. Lewenkopf, E. R. Mucciolo, and A. H. Castro Neto, *Phys. Rev. B* **77**, 081410 (2008).
 - ¹⁷ S. Adam, P. W. Brouwer, and S. Das Sarma, *Phys. Rev. B* **79**, 201404 (2009).
 - ¹⁸ A. Rycerz, J. Tworzydło, and C. Beenakker, *EPL (Europhysics Letters)* **79**, 57003 (2007).
 - ¹⁹ C. Beenakker and H. van Houten, *Solid state physics* **44**, 228 (1991).
 - ²⁰ M. I. Katsnelson, K. S. Novoselov, and A. K. Geim, *Nat Phys* **2**, 620 (2006).
 - ²¹ M. Katsnelson, *The European Physical Journal B-Condensed Matter and Complex Systems* **52**, 151 (2006).